2008

Analytical Expression for the Impedance Response for a Lithium-Ion Cell

Godfrey Sikha
University of South Carolina - Columbia

Ralph E. White
University of South Carolina - Columbia, white@cec.sc.edu

Publication Info

Published in *Journal of the Electrochemical Society*, Volume 155, Issue 12, 2008, pages A893-A902.

Sikha, G. & White, R.E. (2008). Analytical Expression for the Impedance Response for a Lithium-Ion Cell. *Journal of the Electrochemical Society*, *155*(12): A893-A902.
Publisher's Version: http://dx.doi.org/10.1149/1.2976359

Journal of The Electrochemical Society, **155** (12) A893-A902 (2008)
0013-4651/2008/155(12)/A893/10/$23.00 © The Electrochemical Society

Analytical Expression for the Impedance Response for a Lithium-Ion Cell

Godfrey Sikha* **and Ralph E. White****,z**

Department of Chemical Engineering, University of South Carolina, Columbia, South Carolina 29201, USA

An analytical expression to predict the impedance response of a dual insertion electrode cell (insertion electrodes separated by an ionically conducting membrane) is presented. The expression accounts for the reaction kinetics and double-layer adsorption processes at the electrode-electrolyte interface, transport of electroactive species in the electrolyte phase, and insertion of species in the solid phase of the insertion electrodes. The accuracy of the analytical expression is validated by comparing the impedance response predicted by the expression to the corresponding numerical solution. The analytical expression is used to predict the impedance response of a lithium-ion cell consisting of a porous $LiCoO_2$ cathode and mesocarbon microbead anode. A qualitative graphical method to identify the co-existence of solid and solution phase transport limitations in the impedance spectra of insertion electrodes is also discussed in the paper.
 [DOI: 10.1149/1.2976359]

Manuscript submitted April 21, 2008; revised manuscript received August 6, 2008. Published October 6, 2008.

The electrochemical impedance spectroscopy (EIS) technique has long been used as a standard tool to estimate fundamental physical properties, understand reaction mechanisms, and estimate state of charge and state of health in battery systems.[1-4] The interpretation of the impedance spectrum is often based on equivalent circuit-type models that are used to approximate the physiochemical processes that occur in the cell. Although equivalent circuit-type models are computationally efficient for data regression, their applicability is limited by several factors, such as dependence on excessive data sets, nonextendable to different system chemistries, high degree of empiricism required to fit experimental data, and limited phenomenological insight. Physics-based models have a broader scope with better confidence with parameter estimates, but are usually computationally intensive. Moreover, rigorous physics-based impedance models employ numerical schemes to solve for the solution, and the computational time involved in data regression would not be able to meet the application requirements. To optimize model robustness and computational efficiency, researchers have adopted various techniques to reduce mathematical complexity without compromising accuracy, either by using faster solvers adopting advanced solution techniques or by considering only the dominant processes, thereby reducing the variables to be solved. Alternatively, the analytical solution, if available, is always preferred as a computationally efficient solution.

In the list of physics-based impedance models for rechargeable battery systems, most of the rigorous models adopt a numerical scheme to solve the equations.[5-7] Closed-form analytical or symbolic solutions are also presented for such systems but under certain limiting operational and design conditions. Meyers et al.[8] presented an analytical solution for the impedance response of a porous intercalation electrode in the absence of solution phase diffusion limitations. Georen et al.[9] used a similar analytical solution to illustrate the effect of reference-electrode positioning for impedance measurements in metal hydride and $LiMn_2O_4$ electrodes. Devan et al.[10] presented an analytical solution for the impedance response to a symmetric cell consisting of noninsertion porous electrodes. Gomadam et al.[11] used an analytical impedance model for a noninsertion porous electrode without solution phase diffusion limitations for different electrode configurations to estimate physical properties of electrodes. Subramanian et al.[12] presented a symbolic solution procedure to evaluate the impedance response due to the diffusion process in a planar electrode. In our previous work, we presented a methodology to develop a closed-form analytical solution for the impedance response of a single-insertion porous electrode considering the reaction kinetics, double-layer charging, and charge and mass transport processes in solid and solution phases.[13] This work presents a comprehensive analytical model for a cell sandwich consisting of dual-insertion porous electrodes. The model accounts for the reaction kinetics and double-layer adsorption at the interface, potential distribution in the porous electrode and the solution phase, and mass transport in the solution (electrolyte) phase and solid (insertion electrodes) phase. The general form of the analytical expression developed in this work can be used to predict the impedance response of various rechargeable battery systems employing porous insertion electrodes. The expression can also be used to estimate parameters from full-cell/half-cell experimental impedance data obtained on insertion electrode systems.

Mathematical Method and Solution Technique

The schematic of the cell geometry (shown in Fig. 1) consists of a porous anode and cathode separated by an ionically conducting membrane. The pores in the electrodes and the separator are saturated with electrolyte to facilitate ion transport between the electrodes. The main assumptions involved in the mathematical treatment of the cell are: (*i*) one-dimensional (*x*-coordinate) transport of species in the solid matrix-pore continuum, (*ii*) the solid matrix in the insertion electrodes are assumed to be made up of spherical

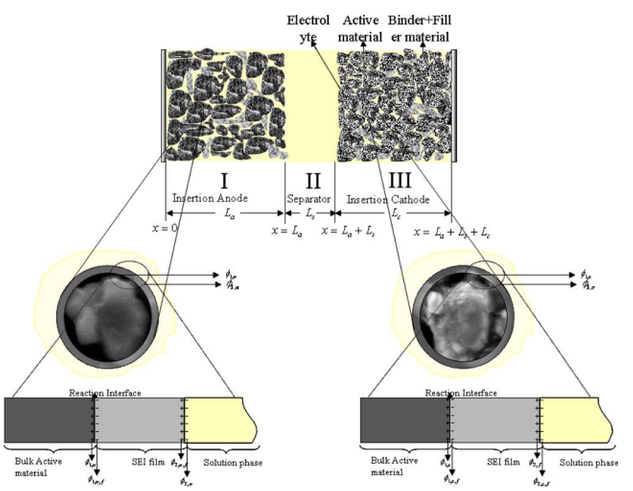

Figure 1. (Color online) Schematic of a cell sandwich containing dual insertion porous electrodes separated by an ionically conducting membrane. The schematic of the magnified version of the single spherical insertion particle and the electrode/electrolyte interface is shown below the cell sandwich.

* Electrochemical Society Fellow.
** Electrochemical Society Active Member.
z E-mail: white@engr.sc.edu

particles and insertion occurs via diffusion in the radial coordinate, (*iii*) the electrochemical reaction of the insertion species is the primary reaction, and any other reactions are ignored, (*iv*) the electrochemical intercalation reaction is assumed to follow Butler Volmer type kinetic reaction rate expression, (*v*) volume changes in the electrode during insertion/de-insertion are ignored, and (*vi*) heat generation and energy balances are ignored. The general electrochemical reaction occurring in either of the insertion electrode in the cell is represented as

$$xM^+ + xe^- + \theta \rightleftharpoons M_x - \theta$$

where θ represents the vacancy in the host insertion material and x represents the stoichiometry of the reaction. The mathematical equations used to describe the processes that occur in the cell are derived from the mass and charge balances in the solid and the electrolyte phases and are presented in our earlier work[13] and are not listed here.

Because the impedance technique is performed using a small amplitude sinusoidal perturbation about a steady state, a linear output response is assumed. Therefore, to obtain the mathematical solution, the system of governing equations can be linearized at the open-circuit conditions. The time-dependent linearized equations are transformed to the Laplace domain (variables topped with a "~") and solved in the Laplace domain. The corresponding complex impedance in the frequency domain (variable ω) is evaluated by substituting $s = j\omega$.[10] The assumption $s = j\omega$ also eliminates the transient part of the response in the mathematical solution but includes the sinusoidal steady-state output response.

Equations in the porous insertion electrodes.— The linearized governing equations in the porous electrode, as presented in Eq. 2–5 in Ref. 13, are transformed using the dimensionless variables ($\bar{c}_i$, $\bar{\eta}_i$, $\bar{x}_i$, $\bar{t}_i$) and converted to the Laplace domain to yield two ordinary differential equations (one for the dimensionless concentration $\tilde{\bar{c}}_i$ and the other for the dimensionless overpotential $\tilde{\bar{\eta}}_i$) in each insertion electrode i and are given as

$$\frac{d^2\tilde{\bar{c}}_i}{d\bar{x}_i^2} = \bar{s}_i\tilde{\bar{c}}_i - \Theta_{1,i}\tilde{\bar{\eta}}_i, \quad i = \mathrm{a,c} \tag{1}$$

$$\frac{d^2\tilde{\bar{\eta}}_i}{d\bar{x}_i^2} = -\bar{s}_i\tilde{\bar{c}}_i + (\Theta_{1,i} + \Theta_{2,i})\tilde{\bar{\eta}}_i, \quad i = \mathrm{a,c} \tag{2}$$

where a and c represent the anode and the cathode porous insertion electrode, respectively. The dimensionless parameter $\Theta_{1,i}$ gives the ratio of the solution phase diffusion resistance to the interfacial resistance, and the dimensionless parameter $\Theta_{2,i}$ gives the ratio of the ohmic resistance to the interfacial resistance. The dimensionless Laplace transformed boundary conditions for Eq. 1 and 2 are given by

$$\bar{x}_\mathrm{a} = 0, \quad \frac{d\tilde{\bar{c}}_\mathrm{a}}{dx_\mathrm{a}} = 0, \quad \frac{d\tilde{\bar{\eta}}_\mathrm{a}}{d\bar{x}_\mathrm{a}} = \tilde{\bar{i}}_\mathrm{app}$$

$$\bar{x}_\mathrm{a} = 1, \quad \frac{d\tilde{\bar{c}}_\mathrm{a}}{d\bar{x}_\mathrm{a}} = -\frac{\Theta_{1,\mathrm{a}}}{\Theta_{2,\mathrm{a}}}\frac{F\left(1 + \frac{\sigma_a}{\kappa_a}\right)}{i_\mathrm{app}(1 - t_+^0)}\xi^\star(\bar{s}_\mathrm{a}), \quad \frac{d\tilde{\bar{\eta}}_\mathrm{a}}{d\bar{x}_\mathrm{a}} = -\frac{\sigma_\mathrm{a}}{\kappa_\mathrm{a}}\tilde{\bar{i}}_\mathrm{app} - \frac{d\tilde{\bar{c}}_\mathrm{a}}{dx_\mathrm{a}}$$

$$\bar{x}_\mathrm{c} = 0, \quad \frac{d\tilde{\bar{c}}_\mathrm{c}}{d\bar{x}_\mathrm{c}} = -\frac{\Theta_{1,\mathrm{c}}}{\Theta_{2,\mathrm{c}}}\frac{F\left(1 + \frac{\sigma_c}{\kappa_c}\right)}{i_\mathrm{app}(1 - t_+^0)}\xi^\star(\bar{s}_\mathrm{c}), \quad \frac{d\tilde{\bar{\eta}}_\mathrm{c}}{d\bar{x}_\mathrm{c}} = -\frac{\sigma_\mathrm{c}}{\kappa_\mathrm{c}}\tilde{\bar{i}}_\mathrm{app} - \frac{d\tilde{\bar{c}}_\mathrm{c}}{dx_\mathrm{c}}$$

$$\bar{x}_c = 1, \quad \frac{d\tilde{\bar{c}}_\mathrm{c}}{dx_\mathrm{c}} = 0, \quad \frac{d\tilde{\bar{\eta}}_\mathrm{c}}{d\bar{x}_\mathrm{c}} = \frac{1}{\bar{s}_\mathrm{c}} \tag{3}$$

where $\xi^\star(\bar{s}_\mathrm{a})$ and $\xi^\star(\bar{s}_\mathrm{c})$ are unknown functions in terms of the dimensionless Laplace variable $\bar{s}_\mathrm{a}$ and $\bar{s}_\mathrm{c}$, respectively. The solution to the coupled second-order linear differential equation (Eq. 1 and 2) is given by

$$\begin{bmatrix} \tilde{\bar{c}}_i \\ \tilde{\bar{\eta}}_i \end{bmatrix} = \begin{bmatrix} 1 & 1 \\ \dfrac{\bar{s}_i - \lambda_{1,i}}{\Theta_{1,i}} & \dfrac{\bar{s}_i - \lambda_{2,i}}{\Theta_{1,i}} \end{bmatrix} \times \begin{bmatrix} C_{1,i}\cosh\sqrt{\lambda_{1,i}}\bar{x}_i + C_{2,i}\sinh\sqrt{\lambda_{1,i}}\bar{x}_i \\ C_{3,i}\cosh\sqrt{\lambda_{2,i}}\bar{x}_i + C_{4,i}\sinh\sqrt{\lambda_{2,i}}\bar{x}_i \end{bmatrix}, \quad i = \mathrm{a,c} \tag{4}$$

where $\lambda_{1,i}$ and $\lambda_{2,i}$ are the eigenvalues given as

$$\lambda_{1,i} = \frac{1}{2}(\bar{s}_i + \Theta_{1,i} + \Theta_{2,i} + \sqrt{\bar{s}_i^2 + 2\Theta_{1,i}\bar{s}_i - 2\Theta_{2,i}\bar{s}_i + \Theta_{1,i}^2 + \Theta_{1,i}\Theta_{2,i} + \Theta_{2,i}^2}), \quad i = \mathrm{a,c}$$

$$\lambda_{2,i} = \frac{1}{2}(\bar{s}_i + \Theta_{1,i} + \Theta_{2,i} - \sqrt{\bar{s}_i^2 + 2\Theta_{1,i}\bar{s}_i - 2\Theta_{2,i}\bar{s}_i + \Theta_{1,i}^2 + \Theta_{1,i}\Theta_{2,i} + \Theta_{2,i}^2}), \quad i = \mathrm{a,c} \tag{5}$$

It should be noted that this solution form holds true for the eigenvalue problem with distinct eigenvalues and linearly independent eigenvectors. The solution obtained in Eq. 4 is substituted into the boundary conditions in Eq. 3 to evaluate for the constants $C_{1,i}$, $C_{2,i}$, $C_{3,i}$, $C_{4,i}$. Although the general solution for the variable in the cathode and the anode porous insertion electrode are similar, the constants evaluated are different because of the different types of boundary conditions in each of the porous electrodes. The expressions for the constants in the anode region are evaluated as

$$C_{1,\mathrm{a}} = \frac{\Theta_{1,\mathrm{a}}\tilde{\bar{i}}_\mathrm{app}}{\sqrt{\lambda_{1,\mathrm{a}}}(\lambda_{1,\mathrm{a}} - \lambda_{2,\mathrm{a}})\sinh\sqrt{\lambda_{1,\mathrm{a}}}}\left(\cosh\sqrt{\lambda_{1,\mathrm{a}}} + \frac{\sigma_\mathrm{a}}{\kappa_\mathrm{a}} - \frac{(\bar{s}_\mathrm{a} + \Theta_{1,\mathrm{a}} - \lambda_{2,\mathrm{a}})\nu\sigma_\mathrm{a}}{L_\mathrm{a}^2\mathrm{a}_\mathrm{a}(1 - t_+^0)\beta_\mathrm{a}}\frac{\xi^\star(\bar{s}_\mathrm{a})}{\tilde{\bar{i}}_\mathrm{app}}\right)$$

$$C_{2,\mathrm{a}} = -\frac{\Theta_{1,\mathrm{a}}\tilde{\bar{i}}_\mathrm{app}}{\sqrt{\lambda_{1,\mathrm{a}}}(\lambda_{1,\mathrm{a}} - \lambda_{2,\mathrm{a}})}$$

$$C_{3,\mathrm{a}} = -\frac{\Theta_{1,\mathrm{a}}\tilde{\bar{i}}_\mathrm{app}}{\sqrt{\lambda_{2,\mathrm{a}}}(\lambda_{1,\mathrm{a}} - \lambda_{2,\mathrm{a}})\sinh\sqrt{\lambda_{2,\mathrm{a}}}}\left(\cosh\sqrt{\lambda_{2,\mathrm{a}}} + \frac{\sigma_\mathrm{a}}{\kappa_\mathrm{a}} - \frac{(\bar{s}_\mathrm{a} + \Theta_{1,\mathrm{a}} - \lambda_{1,\mathrm{a}})\nu\sigma_\mathrm{a}}{L_\mathrm{a}^2 a_\mathrm{a}(1 - t_+^0)\beta_\mathrm{a}}\frac{\xi^\star(\bar{s}_\mathrm{a})}{\tilde{\bar{i}}_\mathrm{app}}\right)$$

$$C_{4\mathrm{a}} = \frac{\Theta_{1,\mathrm{a}}\tilde{\bar{i}}_\mathrm{app}}{\sqrt{\lambda_{2,\mathrm{a}}}(\lambda_{1,\mathrm{a}} - \lambda_{2,\mathrm{a}})} \tag{6}$$

The constants evaluated for the cathode region are similar to that presented in Eq. (24) in Ref. 13 and are evaluated as

$$C_{1,\mathrm{c}} = -\frac{\Theta_{1,\mathrm{c}}\tilde{\bar{i}}_\mathrm{app}}{\sqrt{\lambda_{1,\mathrm{c}}}(\lambda_{1,\mathrm{c}} - \lambda_{2,\mathrm{c}})\sinh(\sqrt{\lambda_{1,\mathrm{c}}})} - \frac{C_{2,\mathrm{c}}}{\tanh\sqrt{\lambda_{1,\mathrm{c}}}}$$

$$C_{2,\mathrm{c}} = \frac{\Theta_{1,\mathrm{a}}\tilde{\bar{i}}_\mathrm{app}}{\sqrt{\lambda_{1,\mathrm{c}}}(\lambda_{1,\mathrm{c}} - \lambda_{2,\mathrm{c}})}\left(\frac{\sigma_\mathrm{c}}{\kappa_\mathrm{c}} - \frac{(\bar{s}_\mathrm{c} + \Theta_{1,\mathrm{c}} - \lambda_{2,\mathrm{c}})\nu\sigma}{L_\mathrm{c}^2 a_\mathrm{c}(1 - t_\mathrm{c}^+)\beta_\mathrm{c}}\frac{\xi^\star(\bar{s}_\mathrm{c})}{\tilde{\bar{i}}_\mathrm{app}}\right)$$

$$C_{3,\mathrm{c}} = \frac{\Theta_{1,\mathrm{c}}\tilde{\bar{i}}_\mathrm{app}}{\sqrt{\lambda_{2,\mathrm{c}}}(\lambda_{1,\mathrm{c}} - \lambda_{2,\mathrm{c}})\sinh(\sqrt{\lambda_{2,\mathrm{c}}})} - \frac{C_{4,\mathrm{c}}}{\tanh\sqrt{\lambda_{2,\mathrm{c}}}}$$

$$C_{4,c} = -\frac{\Theta_{1,c}\tilde{i}_{app}}{\sqrt{\lambda_{2,c}}(\lambda_{1,c}-\lambda_{2,c})}\left(\frac{\sigma_c}{\kappa_c} - \frac{(\bar{s}_c + \Theta_{1,c} - \lambda_{1,c})\nu\sigma}{L_c^2 a_c(1-t_c^+)\beta_c}\frac{\xi^\star(\bar{s}_c)}{\tilde{i}_{app}}\right) \quad [7]$$

The term β_i, which appears in the constants in Eq. 6 and 7 as β_a and β_c, respectively, is related to the local impedance ($Z_{loc,i}$), which is the combined impedance response of single particle ($Z_{p,i}$) and the film surrounding the particle. The single-particle impedance arises from the diffusion of Li in the spherical particles of the solid matrix, charge transfer, and double-layer adsorption at the particle film interface and film impedance arises from the resistance and capacitance of the film surrounding the spherical particle. The local impedance is given as[13]

$$Z_{loc,i} = \frac{1}{F\beta_i}s_i C_{film,i} + \frac{1}{Z_{p,i} + R_{film,i}}, \quad i = a,c \quad [8]$$

$$Z_{p,i} = \frac{1}{s_i C_{dl,i} + (1/R_{ct,i} + R_{dif,i}/Y_{s,i})}, \quad i = a,c \quad [9]$$

where $R_{ct,i}$ and $R_{dif,i}$ are charge transfer resistance and solid phase diffusion resistance, respectively. The expressions for the dimensionless concentration and overpotential can now be explicitly expressed when the values of the constants (Eq. 6 and 7) are substituted into the general solution. These expressions will still retain the unknown constants $\xi^\star(\bar{s}_a)$ and $\xi^\star(\bar{s}_c)$, which will be evaluated by solving for the dimensionless concentration and overpotential in the separator region.

Equations in the separator region.— The dimensionless variables $\bar{c}_i$ and $\bar{\eta}_i$ are decoupled in the separator region because of the absence of the reaction term in the electrolyte mass balance equation. The dimensionless governing equations in the Laplace domain for the mass and charge balances are given in Eq. 10 and 11, respectively

$$\frac{d^2\tilde{\bar{c}}_i}{d\bar{x}_i^2} = \bar{s}_i\tilde{\bar{c}}_i, \quad i = s \quad [10]$$

$$\frac{d\tilde{\bar{\eta}}_i}{d\bar{x}_i} + \frac{d\tilde{\bar{c}}_i}{d\bar{x}_i} = \tilde{i}_{app} \quad [11]$$

and the corresponding dimensionless Laplace transformed boundary conditions are given as

$$\bar{x}_s = 0, \quad \frac{d\tilde{\bar{c}}_s}{d\bar{x}_s} = \Theta_3\xi^\star(\bar{s}_a)$$

$$\bar{x}_s = 1, \quad \frac{d\tilde{\bar{c}}_s}{d\bar{x}_s} = \Theta_3\xi^\star(\bar{s}_c) \quad [12]$$

The general solution for Eq. 10 is given as

$$\tilde{\bar{c}}_s = C_{1,s}\cosh\sqrt{\bar{s}_s}\bar{x}_s + C_{2,s}\sinh\sqrt{\bar{s}_s}\,x_s \quad [13]$$

The value of the constants $C_{1,s}$ and $C_{2,s}$ are evaluated by substituting the general solution given in Eq. 13 in the boundary conditions defined in Eq. 12 and solving for the resulting algebraic equations

$$C_{1,s} = \frac{\Theta_3}{\sqrt{s_s}\sinh\sqrt{s_s}}[\xi^\star(\bar{s}_c) - \xi^\star(\bar{s}_a)\cosh\sqrt{s_s}]$$

$$C_{2,s} = \Theta_3\frac{\xi^\star(\bar{s}_c)}{\sqrt{s_s}} \quad [14]$$

The derivative of the dimensionless concentration is evaluated from Eq. 13 and substituted back into Eq. 11 to evaluate for the dimensionless overpotential $\tilde{\bar{\eta}}_s$ in the separator region. Upon integration and substituting the reference condition $[\bar{\eta}_s(\bar{x}_s = 1) = 0]$, Eq. 11 can be evaluated for $\tilde{\bar{\eta}}_s$ as

$$\tilde{\bar{\eta}}_s = \tilde{i}_{app}\bar{x}_s - 1 + \tilde{\bar{c}}|_{\bar{x}_s=1} - \tilde{\bar{c}}_s \quad [15]$$

The value for $\tilde{\bar{c}}_s$ and $\tilde{\bar{c}}_s|_{\bar{x}_s=1}$ can be evaluated from Eq. 13.

Evaluation of the constants $\xi^\star(\bar{s}_a)$ and $\xi^\star(\bar{s}_c)$.— Knowing the expressions for the dimensionless concentration in the separator region, the constants $\xi^\star(\bar{s}_a)$ and $\xi^\star(\bar{s}_c)$ can be evaluated based on the condition that (*i*) the concentration is continuous at the anode porous electrode/separator interface and (*ii*) the concentration is also continuous at the separator/porous cathode electrode interface, and is mathematically given by, respectively

$$-\frac{\Theta_{2,a}L_a(1-t_+^0)}{\Theta_{1,a}\nu F D_a^{eff}(1+\sigma_a^{eff}/\kappa_a^{eff})}\tilde{\bar{c}}_a|_{\bar{x}_a=1} = \frac{L_s}{\Theta_3 D_s^{eff}}\tilde{\bar{c}}_s|_{\bar{x}_s=0} \quad [16]$$

$$-\frac{\Theta_{2,c}L_c i_{app}(1-t_+^0)}{\Theta_{1,c}\nu F D_c^{eff}(1+\sigma_c^{eff}/\kappa_c^{eff})}\tilde{\bar{c}}_c|_{\bar{x}_c=0} = \frac{L_s}{\Theta_3 D_s^{eff}}\tilde{\bar{c}}_s|_{\bar{x}_s=1} \quad [17]$$

The expressions for $\tilde{\bar{c}}_a|_{\bar{x}_a=1}$ and $\tilde{\bar{c}}_c|_{\bar{x}_c=0}$ are evaluated from Eq. 4 while $\tilde{\bar{c}}_s|_{\bar{x}_s=0}$ and $\tilde{\bar{c}}_s|_{\bar{x}_s=0}$ are evaluated from Eq. 13. The resulting algebraic equations (16 and 17) are simultaneously solved to obtain explicit expressions for $\xi^\star(\bar{s}_a)$ and $\xi^\star(\bar{s}_c)$. The explicit evaluation of $\xi^\star(\bar{s}_a)$ and $\xi^\star(\bar{s}_c)$ is lengthy and involves multiple algebraic manipulations to get a concise form. The expressions for $\xi^\star(\bar{s}_a)$ and $\xi^\star(\bar{s}_c)$ are given as

$$\xi^\star(\bar{s}_a) = \frac{\Lambda_{1,a} + \frac{\Lambda_{1,c}}{\Lambda_{2,c}}\Lambda_3}{\Lambda_{2,a} - \frac{1}{\Lambda_{2,c}}\Lambda_3^2} \quad [18]$$

$$\xi^\star(\bar{s}_c) = \frac{\Lambda_{1,c} + \frac{\Lambda_{1,a}}{\Lambda_{2,a}}\Lambda_3}{\Lambda_{2,c} - \frac{1}{\Lambda_{2,a}}\Lambda_3^2} \quad [19]$$

where the constants $\Lambda_{1,i}$, $\Lambda_{2,i}$, and Λ_3 are given as

$$\Lambda_{1,i} = -\frac{L_i^3 a_i\tilde{i}_{app}(1-t_+^0)\beta_i}{\sigma_i^{eff}\nu_+ D_i^{eff}(\lambda_{1,i}-\lambda_{2,i})}\left[\left(\frac{1}{\sqrt{\lambda_{2,i}}\sinh\sqrt{\lambda_{2,i}}} - \frac{1}{\sqrt{\lambda_{1,i}}\sinh\sqrt{\lambda_{1,i}}}\right) + \frac{\sigma_i^{eff}}{\kappa_i^{eff}}\left(\frac{1}{\sqrt{\lambda_{2,i}}\tanh\sqrt{\lambda_{2,i}}} - \frac{1}{\sqrt{\lambda_{1,i}}\tanh\sqrt{\lambda_{1,i}}}\right)\right], \quad i = a,c$$

$$\Lambda_{2,i} = \frac{L_i}{D_i^{eff}(\lambda_{1,i}-\lambda_{2,i})}\left\{\frac{s_i - \lambda_{2,i} + \Theta_{1,i}}{\sqrt{\lambda_{1,i}}\tanh\sqrt{\lambda_{1,i}}} - \frac{s_i - \lambda_{1,i} + \Theta_{1,i}}{\sqrt{\lambda_{2,i}}\tanh\sqrt{\lambda_{2,i}}}\right\} + \Lambda_3\cosh\sqrt{\bar{s}_s}, \quad i = a,c$$

$$\Lambda_3 = \frac{L_s}{\sqrt{s_s}D_s^{eff}\sinh\sqrt{s_s}} \quad [20]$$

Evaluation of cell impedance.— The impedance of the cell sandwich is the difference in the solid phase potential between the current collector/insertion cathode interface and the current collector/insertion anode interface and is given as

$$Z_{\text{cell}} = -\frac{\tilde{\Phi}_{1,c}|_{\bar{x}_c=1} - \tilde{\Phi}_{1,a}|_{\bar{x}_a=0}}{\tilde{i}_{\text{app}}} \quad [21]$$

The expressions for $\tilde{\Phi}_{1,a}$ and $\tilde{\Phi}_{1,c}$ are evaluated from the overpotentials in the anode $\tilde{\bar{\eta}}_a$ and cathode $\tilde{\bar{\eta}}_c$, respectively. The relation between $\tilde{\Phi}_{1,i}$ and $\tilde{\bar{\eta}}_i$ is given in Eq. 44 in Ref. 13 and the expression for $\tilde{\Phi}_{1,i}$ can be written as

$$\frac{d^2\tilde{\Phi}_{1,i}}{d\bar{x}_i^2} = -\frac{L_i^3 a_i F \beta}{\sigma_c^{\text{eff}^2}} \tilde{\bar{\eta}}_i, \quad i = \text{a,c} \quad [22]$$

Upon integrating Eq. 22 twice, $\tilde{\Phi}_{1,i}$ is evaluated as

$$\tilde{\Phi}_{1,i} = -\frac{L_i^3 a_i F \beta_i}{\sigma_i^{\text{eff}^2}} \iint \tilde{\bar{\eta}}_i d\bar{x}_i d\bar{x}_i + C_{7,i}\bar{x}_i + C_{8,i}, \quad i = \text{a,c} \quad [23]$$

To evaluate the constants $C_{7,i}$, and $C_{8,i}$ in the cathode region, the following boundary conditions are used

$$\bar{x}_c = 0, \quad \tilde{\Phi}_{1,c} = -\frac{L_c}{\sigma_c^{\text{eff}}} \tilde{\bar{\eta}}_c|_{\bar{x}_c=0}, \quad \text{(reference point } \tilde{\Phi}_{2,c}|_{\bar{x}_c=0} = 0)$$

$$\bar{x}_c = 1, \quad \frac{d\tilde{\Phi}_{1,c}}{d\bar{x}_c} = -\frac{L_c \tilde{i}_{\text{app}}}{\sigma_c^{\text{eff}}}, \quad \left(\frac{d\tilde{\Phi}_{2,c}}{d\bar{x}_c}\bigg|_{\bar{x}_c=1} = 0\right) \quad [24]$$

The value of $\tilde{\bar{\eta}}_c|_{\bar{x}_c=0}$ in the above expression is evaluated by substituting $\bar{x}_i = 0$ for $\tilde{\bar{\eta}}_i$ in Eq. 4 for $i = c$. The constants $C_{7,c}$ and $C_{8,c}$ are evaluated by substituting the expression for $\tilde{\bar{\eta}}_i$ from Eq. 4 in Eq. 23 and applying the boundary conditions given in Eq. 24

$$C_{7,c} = -\frac{L_c \tilde{i}_{\text{app}}}{\sigma_c^{\text{eff}}}\left(1 - \frac{\bar{s}_c L_c^2 a_c F \beta_c}{\sigma_c^{\text{eff}} \lambda_{1,c} \lambda_{2,c}}\right)$$

$$C_{8,c} = -\frac{L_c}{\sigma_c^{\text{eff}}}\left[\frac{\bar{s}_c - \lambda_{1,c}}{\Theta_{1,c}} C_{1,c}\left(1 - \frac{L_c^2 a_c F \beta_c}{\sigma_c^{\text{eff}} \lambda_{1,c}}\right) + \frac{\bar{s}_c - \lambda_{2,c}}{\Theta_{1,c}} C_{3,c} \times \left(1 - \frac{L_c^2 a_c F \beta_c}{\sigma_c^{\text{eff}} \lambda_{2,c}}\right)\right] \quad [25]$$

Similarly, to evaluate the constants $C_{7,i}$ and $C_{8,i}$ in the anode region, the following boundary conditions are used

$$\bar{x}_a = 0, \quad \frac{d\tilde{\Phi}_{1,a}}{d\bar{x}_a} = -\frac{L_c i_{\text{app}}}{\sigma_a^{\text{eff}}}, \quad \left(\frac{d\tilde{\Phi}_{2,a}}{d\bar{x}_a}\bigg|_{\bar{x}_a=0} = 0\right)$$

$$\bar{x}_a = 1, \quad \tilde{\Phi}_{1,a} = \tilde{\Phi}_{2,a}|_{\bar{x}_a=1} - \frac{L_a}{\sigma_a^{\text{eff}}} \tilde{\bar{\eta}}_a|_{\bar{x}_a=1} \quad [26]$$

The value of $\tilde{\Phi}_{2,a}|_{\bar{x}_a=1}$ is evaluated using the fact that $\tilde{\Phi}_{2,a}|_{\bar{x}_a=1} = \tilde{\Phi}_{2,s}|_{\bar{x}_s=0}$. Also we know $\tilde{\Phi}_{2,s}|_{\bar{x}_s=0} = -L_s \tilde{\bar{\eta}}_s|_{\bar{x}_s=0}/\kappa_s$. The value for $\tilde{\bar{\eta}}_s|_{\bar{x}_s=0}$ is evaluated using Eq. 15 as

$$\tilde{\bar{\eta}}_s|_{\bar{x}_s=0} = -\tilde{i}_{\text{app}} + \tilde{\bar{c}}_s|_{\bar{x}_s=1} - \tilde{\bar{c}}_s|_{\bar{x}_s=0} \quad [27]$$

Subsequently, $\tilde{\Phi}_{2,a}|_{\bar{x}_a=1}$ can be evaluated. Substituting the expression for $\tilde{\bar{\eta}}_i$ from Eq. 4 in Eq. 23 and using the boundary conditions in Eq. 26, $C_{7,a}$ and $C_{8,a}$ are evaluated to be

$$C_{7,a} = -\frac{L_a \tilde{i}_{\text{app}}}{\sigma_a^{\text{eff}}}\left[1 - \frac{L_a^2 a_a F \beta_a}{\tilde{i}_{\text{app}} \sigma_a^{\text{eff}}}\left(\frac{\bar{s}_a - \lambda_{1,a}}{\Theta_{1,a}\sqrt{\lambda_{1,a}}} C_{2,a} + \frac{\bar{s}_a - \lambda_{2,a}}{\Theta_{1,a}\sqrt{\lambda_{2,a}}} C_{4,a}\right)\right]$$

$$C_{8,a} = -\frac{L_a}{\sigma_a^{\text{eff}}}\left[\frac{\bar{s}_a - \lambda_{1,a}}{\Theta_{1,a}} \chi_{\lambda_1}\left(1 - \frac{L_a^2 a_a F \beta_a}{\sigma_a^{\text{eff}} \lambda_{1,a}}\right) + \frac{\bar{s}_a - \lambda_{2,a}}{\Theta_{1,a}} \chi_{\lambda_2} \times \left(1 - \frac{L_a^2 a_a F \beta_a}{\sigma_a^{\text{eff}} \lambda_{2,a}}\right)\right] + \frac{L_s i_{\text{app}}}{\kappa_s}\left(1 + \frac{\tilde{\bar{c}}_s|_{\bar{x}_s=0} - \tilde{\bar{c}}_s|_{\bar{x}_s=1}}{\tilde{i}_{\text{app}}}\right) - C_{7,a} \quad [28]$$

where χ_{λ_1} and χ_{λ_2} are given as

$$\chi_{\lambda_1} = C_{1,a} \cosh\sqrt{\lambda_{1,a}} + C_{2,a} \sinh\sqrt{\lambda_{1,a}}$$

$$\chi_{\lambda_2} = C_{3,a} \cosh\sqrt{\lambda_{2,a}} + C_{4,a} \sinh\sqrt{\lambda_{2,a}} \quad [29]$$

Substituting the values for $C_{7,a}, C_{8,a}$ in the integrated form of Eq. 23 for the anode ($i = a$) and evaluating the same expression at $\bar{x}_a = 0$ yields an expression for $\tilde{\Phi}_{1,a}|_{\bar{x}_a=0}$. Similarly, substituting the values of $C_{7,c}, C_{8,c}$ in the integrated form of Eq. 23 for the cathode ($i = c$) and evaluating the expression at $\bar{x}_c = 1$ yields an expression for $\tilde{\Phi}_{1,c}|_{\bar{x}_c=1}$. The evaluated expressions for $\tilde{\Phi}_{1,a}|_{\bar{x}_a=0}$ and $\tilde{\Phi}_{1,c}|_{\bar{x}_c=1}$ after algebraic simplification are given as follows

$$\tilde{\Phi}_{1,a}|_{\bar{x}_a=0} = -\frac{L_a^3 a_a F \beta_a}{\sigma_a^{\text{eff}^2}}\left(\frac{\bar{s}_a - \lambda_{1,a}}{\Theta_{1,a}\lambda_{1,a}} C_{1,a} + \frac{\bar{s}_a - \lambda_{2,a}}{\Theta_{1,a}\lambda_{2,a}} C_{3,a}\right) + C_{8,a} \quad [30]$$

$$\tilde{\Phi}_{1,c}|_{\bar{x}_c=1} = \frac{L_c^3 a_c F \beta_c}{\sigma_c^{\text{eff}^2}}\left[\frac{\bar{s}_c - \lambda_{1,c}}{\Theta_{1,c}\lambda_{1,c}}(C_{1,c} \cosh\sqrt{\lambda_{1,c}} + C_{2,c} \sinh\sqrt{\lambda_{1,c}}) + \frac{\bar{s}_c - \lambda_{2,c}}{\Theta_{1,c}\lambda_{2,c}}(C_{3,c} \cosh\sqrt{\lambda_{2,c}} + C_{4,c} \sinh\sqrt{\lambda_{2,c}})\right] + C_{7,c} + C_{8,c} \quad [31]$$

The overall impedance of the cell sandwich, Z_{cell} is evaluated by substituting the values for $\tilde{\Phi}_{1,a}|_{\bar{x}_a=0}$ from Eq. 30 and $\tilde{\Phi}_{1,c}|_{\bar{x}_c=1}$ from Eq. 31 in the cell impedance expression given in Eq. 21. Equations 21, 30, and 31 together should be used to evaluate the impedance response of a dual insertion porous electrode cell.

Results and Discussion

The impedance response predicted using the analytical solution was compared to the predictions from the numerical solution for the same set of equations and is presented in Fig. 2 and 3. The numerical solution was obtained by solving Eq. 1 and 2 along with the boundary conditions defined in Eq. 3 using Comsol Multiphysics. For solving the one-dimensional numerical problem in Comsol Multiphysics, each of the anode, cathode, and the separator domain were discretized to 100 node points. The complex impedance spectrum were evaluated for a range of frequencies using the in-built parametric solver tool in Comsol Multiphysics. The parameters used for the simulation correspond to the material and design properties of the lithium-ion pouch cell from Mine Safety Appliances, which consisted of $LiCoO_2$ cathode and mesocarbon microbead 2528 anode, separated by a Celgard 2320 porous membrane. The electrolyte used in the cell was a solution of 1 M $LiPF_6$ salt dissolved in a mixture of ethylene carbonate/propylene carbonate/ethyl methyl carbonate/diethyl carbonate solvent. The values for the parameters used in the model are presented in Table I.

Figure 2 shows the complex plane impedance (Nyquist) predictions from the analytical solution for a range of frequencies (10^5–10^{-4} Hz), while Fig. 3 shows the corresponding phase and magnitude of the impedance as a function of frequency in a semilog plot (Bode). Both these graphical representations revealed excellent agreement between the numerical and analytical solutions for various values of states of charge of the full cell used in the simulations (see Fig. 4). The state of charge (SOC) of the full cell is used to

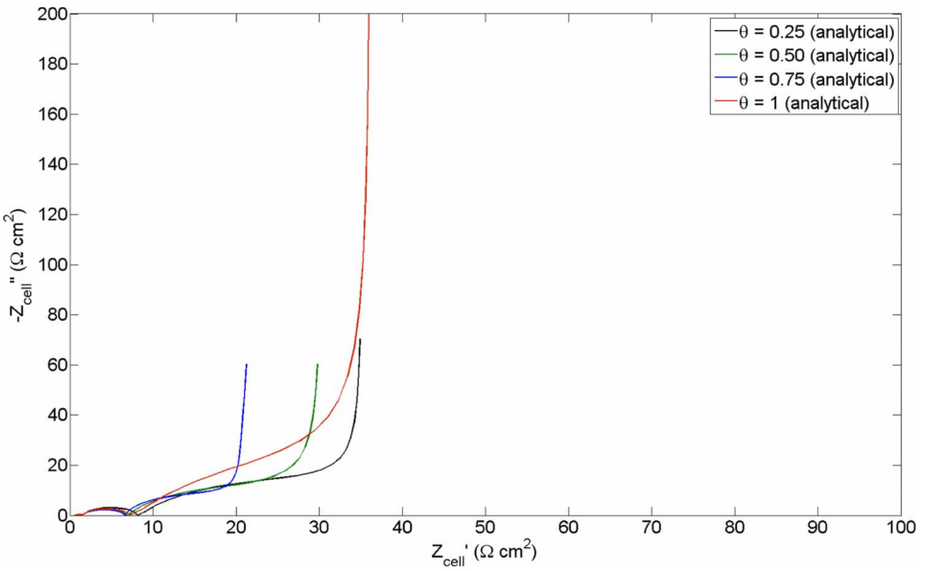

Figure 2. (Color online) Complex plane impedance plot (Nyquist) showing the cell impedance (Z_{cell}) predictions obtained from the analytical solution for different states of charge of the full cell. The impedance values were simulated at 100 evenly spaced logarithmic frequency points between 10^6 and 10^{-4} Hz.

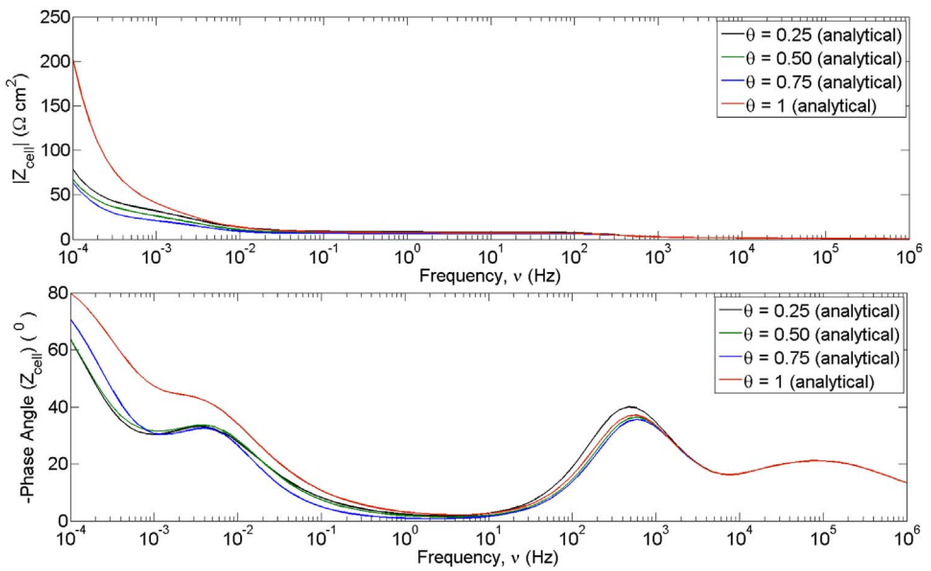

Figure 3. (Color online) Bode plot showing the magnitude (top) and phase angle (bottom) of the cell impedance obtained from the analytical solution for different states of charge of the full cell. The magnitude and phase angle values were simulated at 100 evenly spaced logarithmic frequency points between 10^6 and 10^{-4} Hz.

estimate the values for the initial stoichiometries of the anode z_a^{ini} and the cathode z_c^{ini} in the model. If we assume a perfectly balanced cell, the full-cell SOC is related to z_a^{ini} and z_c^{ini} as

$$\text{SOC} = \frac{z_c^{max} - z_c^{ini}}{z_c^{max} - z_c^{min}} = \frac{z_a^{ini} - z_a^{min}}{z_a^{max} - z_a^{min}} \quad [32]$$

where z_i^{min} and z_i^{max} correspond to the minimum and maximum stoichiometries for the individual electrode. The analytical solution was evaluated at 100 equal logarithmically spaced frequencies between 10^5 and 10^{-4} Hz using Matlab, and the numerical solution was evaluated the same way using Comsol Multiphysics. The computational time for the analytical solution at 50% SOC was ~0.142 s, while the corresponding time for the numerical solution was 27.24 s in a 2.8 GHz, Xeon processor, indicating an improvement in run time by at least two orders of magnitude for the analytical solution. Figure 4 plots the error between the predictions from the numerical and analytical solutions. The errors in the real and the imaginary parts of the cell impedance (given by Σ' and Σ'', respectively) are plotted as a function of frequency in Fig. 4 and are calculated using

$$\Sigma' = Z'_{cell}|_{analytic} - Z'_{cell}|_{numeric}$$

$$\Sigma'' = Z''_{cell}|_{analytic} - Z''_{cell}|_{analytic} \quad [33]$$

where Z'_{cell} and Z''_{cell} represent the real and imaginary part of the impedance spectrum of the cell, respectively. The error between the analytical and numerical solutions is on the order of 10^{-7} and at least six orders of magnitude smaller than the point values, indicating an excellent quantitative agreement between the numerical and the analytical solution.

Figure 5 shows the individual contribution from the anode, cathode, and the separator toward the full-cell impedance spectrum. The impedance spectrum shown in Fig. 5 was simulated at 50% SOC of the full cell. For the parameter values used in this simulation, the impedance contribution from the separator is observed to be negligible as compared to the contribution from the anode or cathode. The complex plane impedance spectrum for the anode and cathode display a similar trend; two arcs in the high mid-frequency regime (10^6–10 Hz), a Warburg-type response due to the diffusion pro-

Table I. List of parameter values used in the model.

Parameters	$LiCoO_2$	Carbon	Separator
$D_{e,i}$ (m^2/s)	1×10^{-12}[a]	3.7125×10^{-14}[a]	—
σ_i (S/m)	10[a]	100[a]	—
ϵ_i	0.3[a]	0.4382[a]	0.45[a]
ϵ_i^f	0.15[a]	0.0566[a]	—
α_i	0.5[a]	0.5[a]	—
R_i (μm)	8.5[a]	12.5[a]	—
i_i^0 (A/m^2)	10 [assumed]	10 [assumed]	—
$C_{dl,i}$ (Fm^2)	0.2 [assumed]	0.2 [assumed]	—
$C_{film,i}$ (F/m^2)	0.02 [assumed]	0.02 [assumed]	—
$R_{film,i}$ (Ω m^2)	1×10^{-4} [assumed]	5×10^{-4} [assumed]	—
$brug_i$	2.3[a]	4.1[a]	1.5[a]
L_i (μm)	70[a]	73.5[a]	25[a]
x_i^{max}	0.99 [measured]	0.7952 [measured]	—
x_i^{min}	0.52 [measured]	0.01 [measured]	—
Electrolyte parameters			
c_B^0 (mol/m^3)	1000[a]		
κ_i (S/m)	10 [assumed]		
D_i (m^2/s)	2.58×10^{-10}[b]		
$f'_{\pm c_B^0}$	1.47×10^{-3}[b]		
$f^f_{\pm c_B^0}$	1.2819[b]		
$t_+^{0\pm c_B^0}$	0.435[b]		
$F(C)$	96,487		
R (J/mol/K)	8.314		
T (K)	298		

[a] Ref. 14.
[b] Ref. 15.

cesses in the solid and solution phases at lower frequencies (10–10^{-3} Hz), and a capacitive-type response at very low frequencies ($<10^{-3}$ Hz) due to intercalation/deintercalation with negligible concentration gradients within the particle. The Bode magnitude (top) and phase angle plot (bottom) presented in Fig. 6 reveals further insight into the impedance spectra of individual cell components. The Bode magnitude plot clearly shows the domination of the anode impedance over the cathode impedance and the negligible contribution from the separator. In the Bode phase plot, the peaks occurring at close to 10^5 and 10^3 Hz in both the cathode and anode correspond to the surface film and charge transfer resistance, respectively. The Bode phase plot also shows a short plateau region for both the anode and cathode between the frequency limits of 10^{-2} and 10^{-3} Hz, corresponding to the semi-infinite diffusion region. At further lower frequencies ($<10^{-3}$ Hz), the phase angle approaches 90° indicating a capacitive-type response typical of insertion electrodes.[8,5,13] The impedance response of the separator is purely resistive above 10 Hz and also approaches a resistive behavior at very low frequencies ($\sim 10^{-4}$ Hz). Between these frequency ranges, the impedance of the separator reveals two closely overlapping time constants due to the electrolyte transport processes in the separator region. In addition, the Bode phase plot for the anode also shows a distinct third peak at around $\sim 2 \times 10^{-3}$ Hz, before the transition to the low-frequency capacitive behavior. In the cathode, a similar but subtle peak at $\sim 9 \times 10^{-3}$ Hz is observed, although the phase angle varies monotonically with frequency. The appearance of this third peak is due to the domination of the impedance from solution phase transport processes over the solid phase diffusion processes in that frequency range. Apparently, this domination is severe and extends to lower frequencies in the anode than the cathode. The solution phase diffusion limitations are less dominant in the cathode compared to the anode because of the larger value of $D_i^0 \epsilon_i^{brug}$ in the cathode region (discussed in the next section). Larger values of solid phase diffusion resistance, R_{dif} shifts the low-frequency capacitive-type behavior observed in intercalation electrodes to lower frequency range. For the parameters used in the model, at 50% SOC, the value of R_{dif} for the anode and cathode was calculated to be 299.09 and 4.152 Ω cm^2, respectively.

Effects of solid and solution phase diffusion limitations in insertion electrodes.— The effect of various parameters in the model, such as exchange current density, double-layer capacitance, and solid and solution phase diffusion coefficients, are discussed for similar systems by Doyle et al.[5] and Dees et al.[7] and will not be reiterated here. However, previous works have paid minimal attention to identifying the relative contribution of solution and solid phase processes toward the overall impedance spectrum. In the impedance spectra of insertion electrode systems, the effect of solution and solid phase transport processes are often closely overlapped in the low-frequency region and difficult to isolate. This situation also complicates the accurate estimation of solid and solution phase diffusion coefficients using traditional techniques.[13] Most of the EIS experimental impedance data were analyzed using the complex plane impedance plot (Nyquist), which has good sensitivity to various processes that occur at different frequency ranges based on the

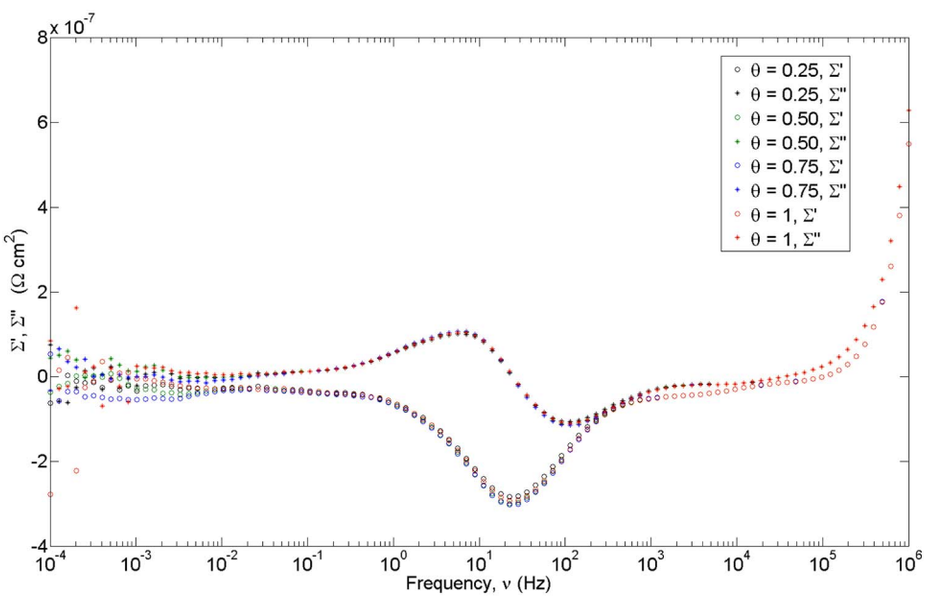

Figure 4. (Color online) Plot showing the error difference between the analytical and the numerical solution of: the real value of the complex impedance given by Σ′, and the imaginary value of the complex impedance given by Σ″ for different states of charge of the full cell. The open circle denotes the error difference in the real values of the complex impedance, while the closed circles denote the error difference in the imaginary values of the complex impedance.

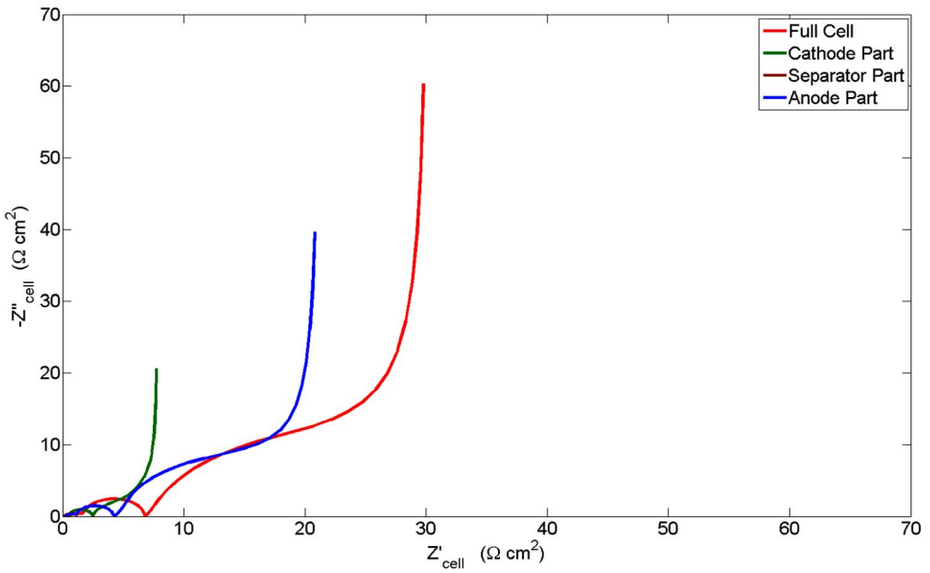

Figure 5. (Color online) Complex plane impedance plot showing the contribution of the individual porous insertion electrodes and the separator toward the overall impedance of the cell, Z_{cell}. The impedance spectrum shown for each component is estimated at a full cell SOC value of 0.5. The impedance values are simulated using the analytical solution at 100 evenly spaced logarithmic frequency points between 10^6 and 10^{-4} Hz.

time constants of each process. However, when the time constants for the solution and solid phase transport processes are in close proximity, the Nyquist plots offers poor sensitivity to these processes. For such situations, analysis using the Bode phase plot was found to be very useful. Figure 7 shows the Bode magnitude and phase plot for the porous anode part of the full cell. The Bode plots for the porous anode is presented here to clearly illustrate the overlap of the impedance spectrum of solution and solid phase transport processes over a particular frequency range. The simulated Bode (magnitude and phase) plot for the porous anode is presented for different values of diffusion coefficient of salt in the electrolyte. The value for the solid phase diffusion coefficients of Li into the insertion anode electrode was held constant at a value of $D_{\theta,a} = 3.7125 \times 10^{-14}$ m^2/s in all these simulations. The Bode magnitude plot (top) shows an increased value for the impedance in the low-frequency region for lower values of salt diffusion coefficient; however, it does not display sensitivity toward the various processes in the cell. In the Bode phase plot (bottom), a peak in the low-frequency region (<1 Hz) is seen for cases b–e. The presence of the peak indicates the dominance of the impedance contribution from solution phase transport process over the solid phase diffusion process in that frequency range. This low-frequency peak vanishes when the impedance contribution from solution phase transport processes is negligible relative to the solid phase diffusion process as seen in case a, where a high value for solution phase diffusion coefficient is used. The Bode phase plot analysis is also useful to identify the extent of the influence of solution phase diffusion process in the overall impedance spectrum. An increase in the sharpness of the peaks (large phase angle values) and a shift in the peak position toward lower frequencies indicates an increased effect of solution phase transport process toward the overall impedance spectrum. The Nyquist plot generally does not offer clear distinction between the solution phase and solid phase diffusion processes in the Warburg slope region. Thus, the Bode phase plots offer a better graphical resolution to distinguish the impedance contribution from solution and solid phase transport processes.

In Fig. 8, the Bode (magnitude and phase) plots show the effect of solid phase diffusion coefficients of Li into the insertion anode electrode, which has solution phase transport limitations. The value for the diffusion coefficient of the salt in electrolyte was fixed at

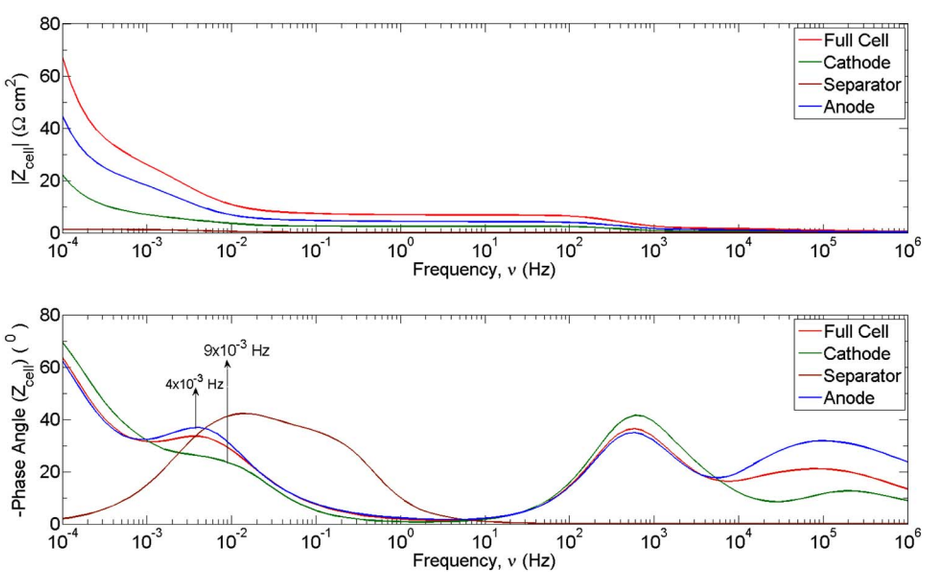

Figure 6. (Color online) Bode plot showing the magnitude (top) and phase angle (bottom) of the impedance of the individual porous insertion electrodes and separator for different states of charge of the full cell. The magnitude and phase values are simulated using the analytical solution at 100 evenly spaced logarithmic frequency points between 10^6 and 10^{-4} Hz.

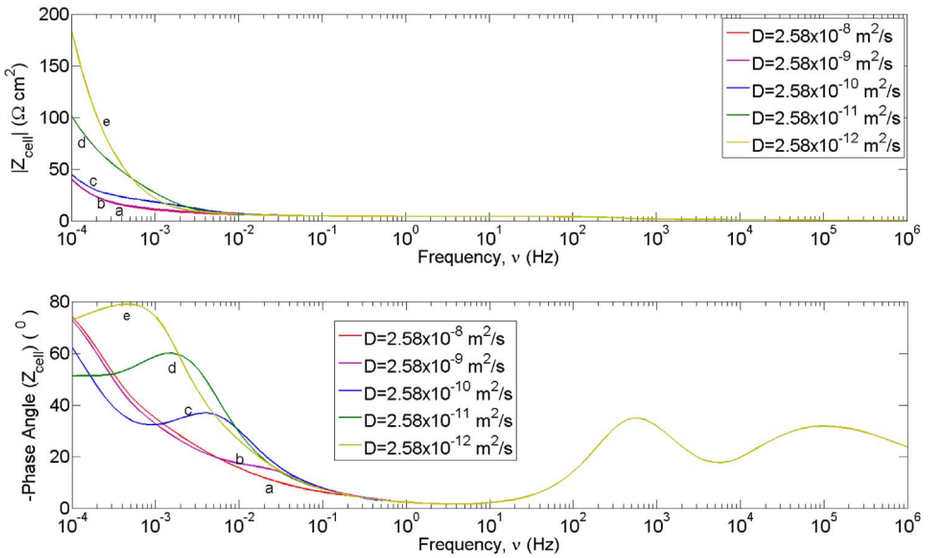

Figure 7. (Color online) Bode magnitude (top) and phase (bottom) plots showing the effect of solution phase diffusion coefficient on the impedance of the anode. The simulations shown are evaluated at the full cell SOC value of 0.5 and the value of the solid phase diffusion coefficient in the anode $D_{\theta,a}$ was fixed at 3.7125×10^{-14} m^2/s. The magnitude and phase values are simulated using the analytical solution at 100 evenly spaced logarithmic frequency points between 10^6 and 10^{-4} Hz.

$D_i = 2.58 \times 10^{-10}$ m^2/s for all the simulations in the plot. As seen in the Bode phase plot (bottom), for all cases (i.e., a–e), the effect of solution phase diffusion is significant, as identified by the peak in the low-frequency region. When the value of the solid phase diffusion coefficient in the anode is decreased, as shown from cases a–e, the sharpness of the peak gets subdued; however, the low-frequency peak (corresponding to the solution phase diffusion process) does not shift and occurs at the same frequency. As discussed in the earlier section, the sharpness of the peak indicates the domination of the solution phase diffusion limitations and in Fig. 8 where the peaks get subdued (i.e., at low values of solid phase diffusion coefficient), the solution phase diffusion processes no longer dominate and the solid phase diffusion processes control the cell impedance. The significance of the solid phase diffusion process is identified by the slope of the curve in the Bode phase plot in the frequency range lower to where the peak is observed. A flat plateau in this region corresponds to the domination of a semi-infinite type of diffusion in the solid phase for the frequency range under consideration (very low values of $D_{\theta,a}$), while sloping profiles indicate the transition-frequency behavior (moderately low values of $D_{\theta,a}$) and the culmination to 90° at low frequencies indicate the domination of the low-frequency capacitive behavior due to intercalation/deintercalation in the absence of concentration gradients (at high values of $D_{\theta,a}$). It should also be realized that at certain states of charge when the slope of the open-circuit potential (OCP) with respect to the concentration is zero (as in two phase coexistence regions), the impedance response reaches a stationary state at low frequencies and the Bode representation will correspond to a resistive behavior at very low frequencies. These graphical identification scenarios will be very useful in qualitatively understanding the various processes that control the cell impedance behavior from the EIS data.

The advantage of impedance spectrum analysis over the conventional dc resistance technique, such as the current interruption method, is the possibility to understand the impedance contribution from various processes in the cells with better resolution. In addition, this technique in combination with rigorous mathematical analysis allows the possibility to clearly identify the impedances from different cell constituents (i.e., electrodes and separators). The breakdown of impedance contribution from various cell components is of critical importance because most experimental EIS measurements are taken on full cells and the contribution from individual cell constituents cannot be directly determined. Specially, in the case

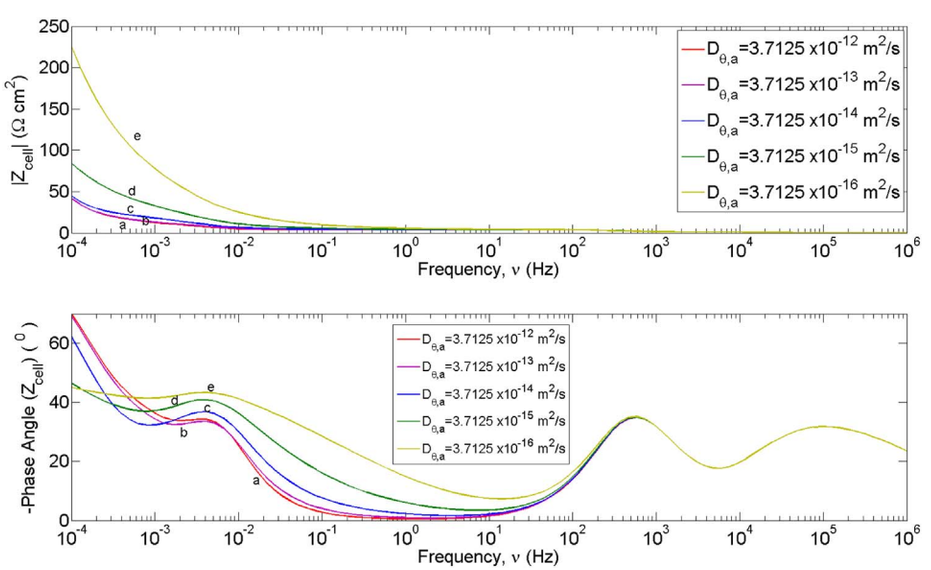

Figure 8. (Color online) Bode magnitude (top) and phase (bottom) plots showing the effect of solid phase diffusion coefficient of Li on the impedance of the anode. The simulations shows are evaluated at the full cell SOC value of 0.5, and the value for the solution phase diffusion coefficient, $D_i = 2.58 \times 10^{-10}$ m^2/s was held constant for all the cases. The magnitude and phase values are simulated using the analytical solution at 100 evenly spaced logarithmic frequency points between 10^6 and 10^{-4} Hz.

of cycling and aging of lithium-ion cells, the overall increase in magnitude of the impedance spectrum with cycling/aging will clearly depict the deterioration process; however, the individual electrode contribution cannot be identified with ease. The analytical solution developed here can be used in conjunction with the EIS data to build an analytical tool that can probe different degradation processes and also identify the contribution from the individual cell constituents toward these processes at various time scales. Such a tool will be very useful for life predictions in modern batteries and design of better electrodes. Our future work will present a detailed analysis of the evaluation of the individual electrode spectrum from full cell electrochemical impedance spectra data.

Conclusions

An analytical solution for the impedance response of a dual-insertion electrode is presented in this work. The results from the analytical solution are validated with the numerical solution evaluated for a lithium-ion system consisting of a $LiCoO_2$ cathode and carbon anode. The analytical expression can be directly used to estimate transport, kinetic, and thermodynamic parameters by comparing to experimental impedance data obtained on full cells with insertion electrodes. The analytical expression is also computationally highly efficient compared to the corresponding numerical solution. The use of Bode phase representation to identify solid and solution phase transport limitations in closely overlapped frequencies is also discussed.

Acknowledgment

Financial support provided by National Reconnaissance Office (NRO) under contract no. NRO-000-03-C-0122 is gratefully acknowledged.

University of South Carolina assisted in meeting the publication costs of this article.

Appendix

Thermodynamic Data for the OCP for the Insertion Electrodes

$LiCoO_2$ insertion electrode.— The OCP of the $LiCoO_2$ insertion electrode was experimentally measured against Li foil in a coin cell using a very low rate (150 h) and fit to the function

$$U_c = \frac{a_{c,0} + \sum_{k=1}^{N=5} a_{c,k}\left(\frac{c_{\theta,c}}{c_{T,c}}\right)^k}{b_{c,0} + \sum_{k=1}^{N=5} b_{c,k}\left(\frac{c_{\theta,c}}{c_{T,c}}\right)^k}$$

where the constants are given as $a_{c,0} = 4.0396$, $a_{c,1} = -32.5724$, $a_{c,2} = 104.8654$, $a_{c,3} = -168.3891$, and $a_{c,4} = 134.6638$, $a_{c,5} = -42.6072$, and $b_{c,0} = 1$, $b_{c,1} = -8.0912$, $b_{c,2} = 26.1404$, $b_{c,3} = -42.1196$, $b_{c,4} = 33.7932$, and $b_{c,5} = -10.7226$.

Carbon insertion electrode.— The OCP of the carbon insertion electrode was experimentally measured against Li foil in a coin cell using a very low rate (150 h) and fit to the function

$$U_a = a_{a,0} + \sum_{k=1}^{N=10} a_{a,k}\left(\frac{c_{\theta,a}}{c_{T,a}}\right)^k$$

where the constants are given as $a_{a,0} = 0.7618$, $a_{a,1} = -22.9218$, $a_{a,2} = 391.6785$, $a_{a,3} = -3667.79902$, $a_{a,4} = 20344.57584$, $a_{a,5} = -70461.1728$, $a_{a,6} = 156433.6149$, $a_{a,7} = -222631.7640$, $a_{a,8} = 196431.2859$, $a_{a,9} = -97849.0694$, and $a_{a,10} = 21038.08558$.

Effective values of conductivity and diffusion coefficient of Li^+ in the electrolyte

The effective diffusion coefficient of the salt in the electrolyte is given by the Bruggeman's relation as

$$D_i^{eff} = D_i^0 \epsilon_i^{brug_i}$$

Similarly the effective conductivities of Li^+ in the solution and the solid phase are also related through the Bruggeman relation as

$$\sigma_i^{eff} = \sigma_i(1 - \epsilon_i - \epsilon_f)^{brug_i}$$

$$\kappa_i^{eff} = \kappa_e \epsilon_i^{brug_i}$$

List of Symbols

a	specific surface area of the porous active material, m^2/m^3
c	solution phase concentration, mol/m^3
$\bar{c}_i$	dimensionless concentration in the porous electrode i = a,c defined as $-[2RT(1 - t_+^0)]/Fi_{iapp}(1/c_B^0 + f_{\pm,c_B^0}/f'_{\pm,c_B^0})\sigma_i^{eff}/L_i(c_i - c_B^0)$
c_θ	solid phase concentration, mol/m^3
c_B^0	initial bulk electrolyte concentration, mol/m^3
C_{dl}	double-layer capacitance of the electrode, F/m^2
C_{film}	capacitance of the film, F/m^2
D_i	diffusion coefficient of the salt in the electrolyte phase, m^2/s
D_θ	diffusion coefficient of Li^+ in the solid phase, m^2/s
$f_\pm$	activity coefficient of Li^+ in the electrolyte
$f'_\pm$	derivative of $f_\pm$ with respect to c, m^3/mol
F	Faraday's constant, 96,487 C/equation
i_0	exchange current density, A/m^2
i_1	local current density in the solid phase, A/m^2
i_2	local current density in the solution phase, A/m^2
$\tilde{i}_{app}$	perturbed current density, A/m^2
i_F	faradaic current density, A/m^2
i_{dl}	double layer current density, A/m^2
i_n	total outward normal current density, A/m^2
L	thickness of the electrode/separator, m
j_n	reaction rate at the pore wall interface, $mol/m^2/s$
r	radial coordinate in an active material particle, m
R	ideal gas constant, J/mol/K
$R_{ct,i}$	charge transfer resistance in the electrode i = a,c defined as $RT/i_{0,i}(\alpha_{a,i} + \alpha_{c,i})F$, Ωm^2
$R_{dif,i}$	solid phase diffusional resistance in electrode i = a,c defined as $-(R_{p,i}/D_{\theta,i}F)(dU_i/dc_{\theta,i}), \Omega m^2$
R_{film}	resistance of the surface film, $\Omega\ m^2$
R_p	radius of the spherical particle, m
s	Laplace variable, s^{-1}
$\bar{s}_i$	dimensionless Laplace variable in the region i given by $\epsilon_i L_i^2 s/D_i^{eff}$
t_+^0	transference number of Li^+ in the electrolyte
t	time, s
$\bar{t}_i$	dimensionless time in region i, $D_i t/\epsilon_i L_i^2$
T	temperature, K
U	open circuit potential, V
x	spatial dimension (distance from the anode), m
$\bar{x}_i$	dimensionless thickness of region i, given by $\bar{x}_a = x/L_a$, $\bar{x}_s = x - L_a/L_s$, $\bar{x}_c = [x - (L_a + L_c)]/L_c$
$Y_{s,i}$	transfer function for the solid phase diffusion in a single particle defined as $\sqrt{s_i R_{p,i}^2/D_{\theta,i}} - \tanh(\sqrt{s_i R_{p,i}^2/D_{\theta,i}})/\tanh(\sqrt{s_i R_{p,i}^2/D_{\theta,i}})$
z_i	stoichiometric coefficient for the electrode i = a,c
Z_{cell}	total impedance of the electrochemical cell, $\Omega\ m^2$

Greek

α	transfer coefficient
ϵ	porosity of the composite electrode/separator
$\bar{\eta}_i$	dimensionless electrochemical reaction over potential in the electrode i = a,c given by $-(\sigma_i/L_i)\ (\phi_{1,i} - \phi_{2,i})$
$\bar{\eta}_s$	value of $\bar{\eta}_i$ in the separator region given by $-\kappa_s\phi_{2,s}/L_s i_{app}$
κ	conductivity of Li^+ in the solution phase, S/m
σ	solid phase electronic conductivity in the electrode i = a,c, S/m
ϕ_1	solid phase potential, V
ϕ_2	solution phase potential, V
$\Theta_{1,i}$	dimensionless parameter describing the ratio of the solution phase resistance to the interfacial resistance in electrode i = a,c defined as $[2RT(1 - t_+^0)^2 L_i]/[vF^2 D_i^{eff}][(1/c_B^0) + (f'_{\pm,c_B^0}/f_{\pm,c_B^0})]/1/L_i a_i F\beta_i$
$\Theta_{2,i}$	dimensionless parameter describing the ratio of the ohmic resistance to the interfacial resistance in electrode i = a,c defined as, $L_i(1/\sigma_i^{eff} + 1/\kappa_i^{eff})/1/L_i a_i F\beta_i$
Θ_3	dimensionless parameter defined as $[2\kappa RT(1 - t_+^0)]/D_i^{eff}F[(1/c_B^0) + (f_{\pm,c_B^0}/f'_{\pm,c_B^0})]$
λ_1, λ_2	eigenvalues as defined in Eq. 5
ν_+	number of cations into which a mole of electrolyte dissociates
v	frequency, Hz
ω	angular frequency, s^{-1}
χ	as defined in Eq. 29

Subscripts

a	anode insertion electrode
c	cathode insertion electrode
i	anode, cathode, or separator region

s	separator
θ	solid phase of the insertion electrode

Superscripts

	dimensionless variable
~	variable in the Laplace domain
eff	effective values
f	fill

References

1. K. Dokko, M. Mohamedi, Y. Fujita, T. Itoh, M. Nishizawa, M. Umeda, and I. Uchida, *J. Electrochem. Soc.*, **148**, A422 (2001).
2. P. Yu, B. N. Popov, J. A. Ritter, and R. E. White, *J. Electrochem. Soc.*, **146**, 8 (1999).
3. M. G. S. R. Thomas, P. G. Bruce, and J. B. Goodenough, *J. Electrochem. Soc.*, **132**, 1521 (1985).
4. J. Fan and P. S. Fedkiw, *J. Power Sources*, **72**, 165 (1998).
5. M. Doyle, J. P. Meyers, and J. Newman, *J. Electrochem. Soc.*, **147**, 99 (2000).
6. Q. Z. Guo, V. R. Subramanian, J. W. Weidner, and R. E. White, *J. Electrochem. Soc.*, **149**, A307 (2002).
7. D. Dees, E. Gunen, D. Abraham, A. Jansen, and J. Prakash, *J. Electrochem. Soc.*, **152**, A1409 (2005).
8. J. P. Meyers, M. Doyle, R. M. Darling, and J. Newman, *J. Electrochem. Soc.*, **147**, 2930 (2000).
9. P. Georen, A.-K. Hjelm, G. Lindbergh, and A. Lundqvist, *J. Electrochem. Soc.*, **150**, A234 (2003).
10. S. Devan, V. R. Subramanian, and R. E. White, *J. Electrochem. Soc.*, **151**, A905 (2004).
11. P. M. Gomadam, J. W. Weidner, T. A. Zawodzinski, and A. P. Saab, *J. Electrochem. Soc.*, **150**, E371 (2003).
12. V. R. Subramanian, V. Boovaragavan, K. Potukuchi, V. D. Diwakar, and A. Guduru, *Electrochem. Solid-State Lett.*, **10**, A25 (2007).
13. G. Sikha and R. E. White, *J. Electrochem. Soc.*, **154**, A43 (2007).
14. K. Kumaresan, G. Sikha, and R. E. White, *J. Electrochem. Soc.*, **155**, A164 (2008).
15. L. O. Valoen and J. N. Reimers, *J. Electrochem. Soc.*, **152**, A882 (2005).